Chapter 3

A systematic study of non-PGM metal hydroxides/oxides toward oxygen electrocatalysis

Outline

Although Pt/C, RuO_2, IrO_2 are highly active for ORR and OER, they suffer degradation and dissolution on prolonged use. Hence the cost and stability are major bottlenecks on the route to commercialization [1]. Significant efforts have been made in the design and development of non-Pt metal group (non-PGM) based catalysts (mostly 1st row transition metals) to meet the three major targets: cost, performance and durability [2]. As already mentioned in Chapter 1, transition metal oxides and hydroxides have come up as very promising categories of catalysts for ORR and OER in alkaline fuel cells. This chapter discusses the synthesis, characterization and electrocatalytic study of three non-PGM metal oxides/hydroxides, viz. Co_3O_4, CeO_2 and $Ni(OH)_2$ along with mixed (hydro)oxides of Co_3O_4/CeO_2, $Ni(OH)_2/CeO_2$ and $Co_3O_4/Ni(OH)_2/CeO_2$. This chapter is the preliminary investigation for the subsequent chapters and is an integral part of the thesis. The chapter is divided into two sections to allow clarity and proper understanding of the experimental findings. The sections are as described below:

Section 3A: A study of (hydro)oxides of Co, Ni and Ce towards oxygen electrocatalysis

This section contains the synthesis and characterization of three graphene supported (hydro)oxides viz. Co_3O_4/GNP, $Ni(OH)_2$/GNP and CeO_2/GNP (GNP=graphene nanoplatelet). The electrochemical properties of these catalysts are studied towards ORR and OER. This chapter helps in identifying cobalt (Co) as the active element for the subsequent chapters along with the indication that integration of CeO_2/GNP could be explored as a beneficial additive for enhancement of electrocatalysis of Co-based (hydro)oxides catalysts.

Section 3B: Tuning the electrocatalytic activity of the bimetallic (hydro)oxides of Co_3O_4 and $Ni(OH)_2$ by integration of CeO_2

In this section, the bimetallic mixed (hydro)oxides Co_3O_4/CeO_2/GNP and $Ni(OH)_2/CeO_2$/GNP have been compared to the trimetallic mixed (hydro)oxide $Co_3O_4/Ni(OH)_2/CeO_2$/GNP towards ORR and OER. The ratio of the active elemets Co and Ni to that of Ce have been placed at 3:1. Experimental results confirm that the combination of Co_3O_4 and CeO_2 exhibits potential application as non-noble electrocatalyst for ORR and OER and paves the path for in-depth exploration of this phenomena in the subsequent chapters.

Both the sections are described in detail.

Section 3A: A study of (hydro)oxides of Co, Ni and Ce towards oxygen electrocatalysis

In this section, we synthesize three (hydro)oxides, viz. Co_3O_4/GNP, $Ni(OH)_2$/GNP and CeO_2/GNP (GNP=graphene nanoplatelet) and these are tested for electrocatalytic ORR and OER. The synthesis procedure is described in Section 2.2.1, 2.2.2 and 2.2.3 respectively.

3A.1 Results and discussion

3A.1.1 Physical characterization

The phase crystallinity of the materials are studied by PXRD analysis. The PXRD of the catalysts and the standard JCPDS reference peaks are presented in Figure 3A.1.

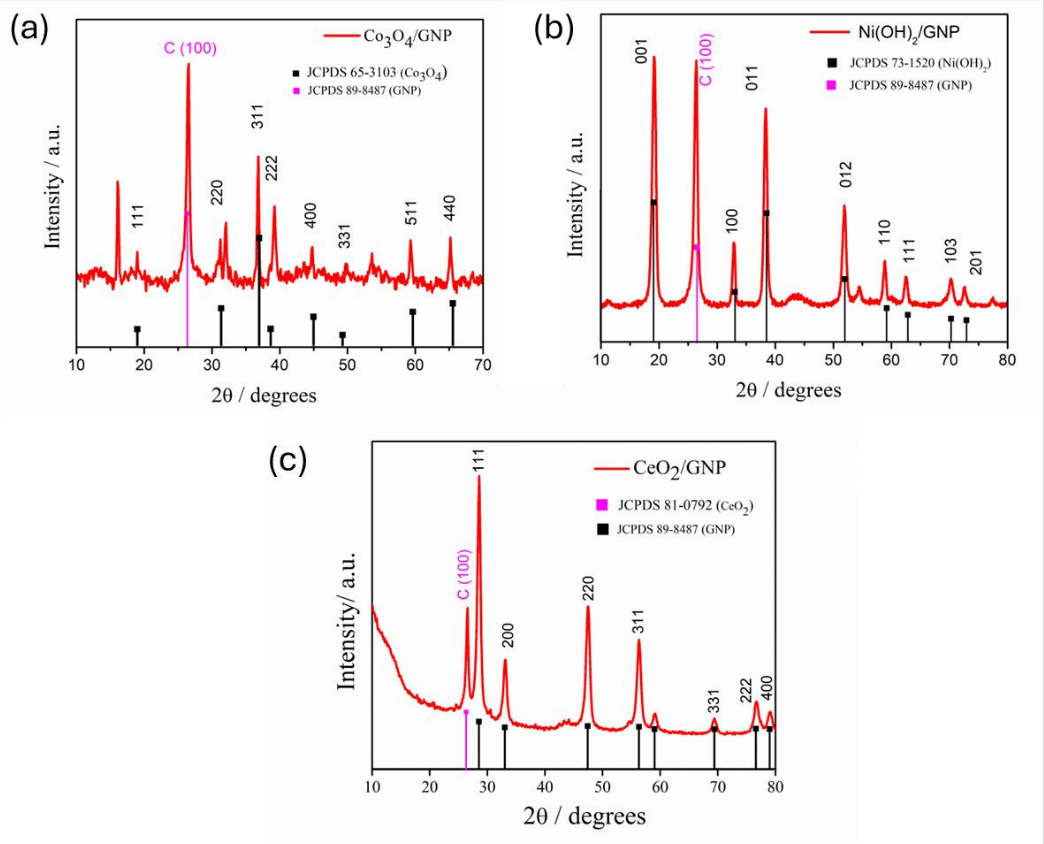

Figure 3A.1. PXRD spectra of (a) Co_3O_4/GNP, (b) $Ni(OH)_2$/GNP, and (c) CeO_2/GNP.

The diffraction patterns reveal that the materials are polycrystalline in nature with sharp and distinguished peaks. The intense peak at 2θ=26.5° (marked as C (100) in magenta pink) in each PXRD spectrum depicts the (100) plane of GNP which comprises 70 wt.% of the catalysts. Figure 3A.1 (a) shows that the diffraction pattern of Co_3O_4/GNP has signals at 2θ= 19.1°, 31.3, 36.9, 38.6°, 44.9, 49.3°, 59.5, 65.4° which corresponds to Miller planes (111), (220), (311), (222), (400), (331), (511) and (440), respectively, characteristic of the spinel Co_3O_4 (JCPDS# 65-3103, crystallizes in the cubic $Fd\bar{3}m$ space group) [3–6]. In Figure 3A.1 (b), the well-defined diffraction peaks for $Ni(OH)_2$/GNP at 2θ =19.2°, 33.2°, 38.6°, 52.1°, 59.3°, 62.9°, 70.4° and 73.0° correspond to the Miller planes (001), (100), (011), (012), (110), (111), (103) and (201) respectively. This is characteristic of hexagonal β-$Ni(OH)_2$ (JCPDS# 73-1520) which confirms the formation of high purity $Ni(OH)_2$ [7]. The prominent peaks in Figure 3A.1 (c) appearing at 2θ = 28.5°, 33.1°, 47.5°, 56.3°, 59.1°, 69.4°, 76.7° and 79.1° coincides well with the crystalline planes of CeO_2 (JCPDS# 81-0792, crystallizes in the cubic $Fm\bar{3}m$ space group) [5,8,9].

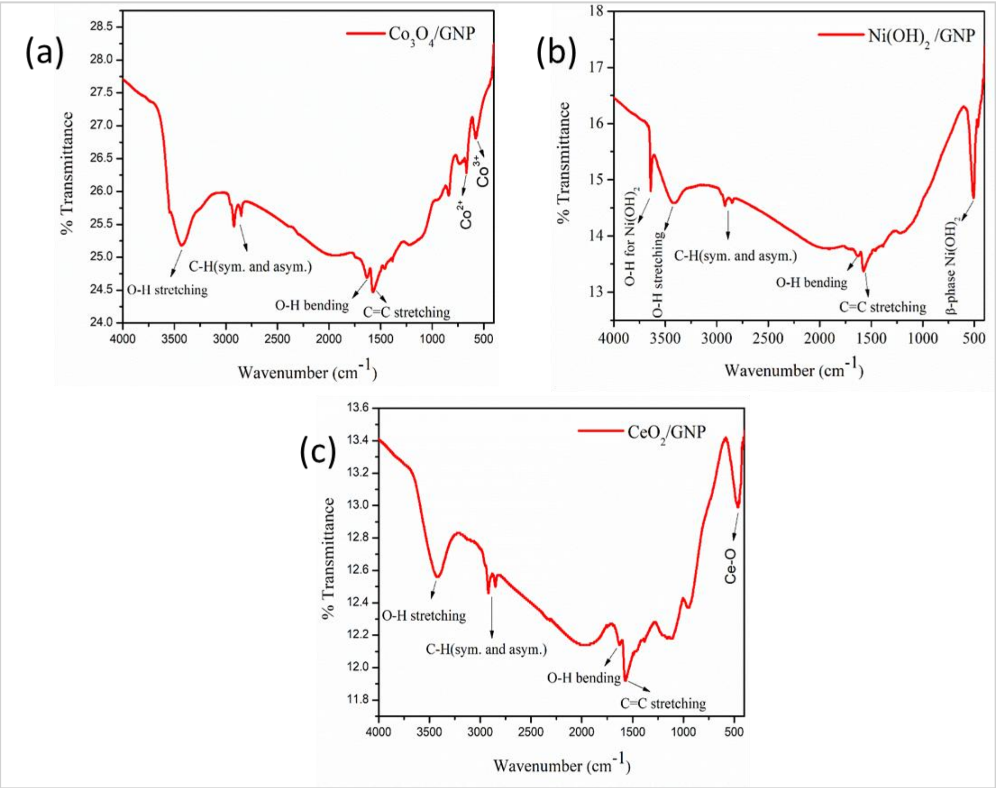

Figure 3A.2. FTIR spectra of (a) Co_3O_4/GNP, (b) $Ni(OH)_2$/GNP, and (c) CeO_2/GNP.

It is to be noted that the Co sample predominantly forms oxide while the Ni sample forms hydroxide phase. This could be due to higher formation constant for Ni-hydroxide than for Ni-oxide. Another reason could be that urea directly converts Co into oxide but it is not strong enough a base to directly convert Ni to oxide. An additional step of calcination is required to convert this Ni hydroxide to Ni oxide.

The FTIR spectra of the synthesized materials are shown in Figure 3A.2. Figure 3A.2 (a–c) shows presence of surface adsorbed H_2O molecules depicted from the intense and broad bands at ~3500 cm^{-1} (for O─H stretching modes) and weak bands at ~1633 cm^{-1} (for O─H bending modes) [5,9,10]. The peaks located at frequencies ~2920 and ~2856 cm−1 are due to C─H symmetric and asymmetric vibrations and at ~1578cm^{-1} is due to the C=C conjugated stretching of the GNP [11]. In Figure 3A.2 (a) the peaks at ~656 and ~565 cm^{-1} can be attributed to Co^{2+} in tetrahedral holes and Co^{3+} in octahedral holes respectively, which are characteristic of Co_3O_4 in its spinel form [5]. In Figure 3A.2 (b), the sharp peak at 3636 cm^{-1} stands for the O─ H stretching vibrations, which is characteristic of $Ni(OH)_2$. The fingerprint region, the 509 cm^{-1} band is related to β-phase of $Ni(OH)_2$ [10]. The presence of a strong peak at ~461 cm^{-1} in Figure 3A.2 (c) is attributed to Ce─O bond [8]. In Figure 3A.2 (d) the FT-IR spectrum exhibited a peak for M–O–M stretching at ~656 $cm^{-1}$and M=O at ~ 570 cm^{-1} [9].

Raman spectra in Figure 3A.3 (a) reveal intense G-band (at ~1350 cm^{-1}) and D-band (at ~1570 cm^{-1}). The G-band depicts E_{2g} phonons arising from in-plane stretching modes of sp^2 C in the GNP framework while the D-band reflects the presence of sp^3 C in the GNP framework [12]. Apart from this, other Raman active vibrational modes, viz. F_{2g} (CeO_2) and A_{1g} (Co_3O_4) are also observed [13–16]. The characteristic peaks of $Ni(OH)_2$ vibrational modes are masked by the intense D- and G-bands. The mass loading of the active metal oxides and hydroxides were confirmed from TGA (in air) analysis shown in Figure 3A.3 (b). There is a weight loss of 70% which confirms that the active mass is 30 wt.%. The 70 wt.% of carbon content or GNP is air-oxidized as CO_2. For all three samples, mass loss around 100 °C is caused by the loss of adsorbed water. For $Ni(OH)_2$, the weight loss between 250 to 400 °C corresponds to conversion of nickel hydroxide into non-stoichiometric nickel oxides like $NiO_{1.5}$. The third region occurring from 400 to 500 °C corresponds to the formation of stoichiometric NiO. For Co_3O_4/GNP, there are two rapid mass loss at 300–400 °C and 450–700 °C. The former is attributed to the thermal decomposition of any residual $Co(OH)_2$ or $CoCO_3$ into Co_3O_4, and the latter is attributed to the combustion of GNP into CO_2. For CeO_2/GNP, a single-step decomposition at ~400 °C comprises primarily of the combustion of GNP. It also implies that CeO_2 is formed in clean oxide phase with no residual hydroxide or carbonate phases as in the case of Ni and Co.

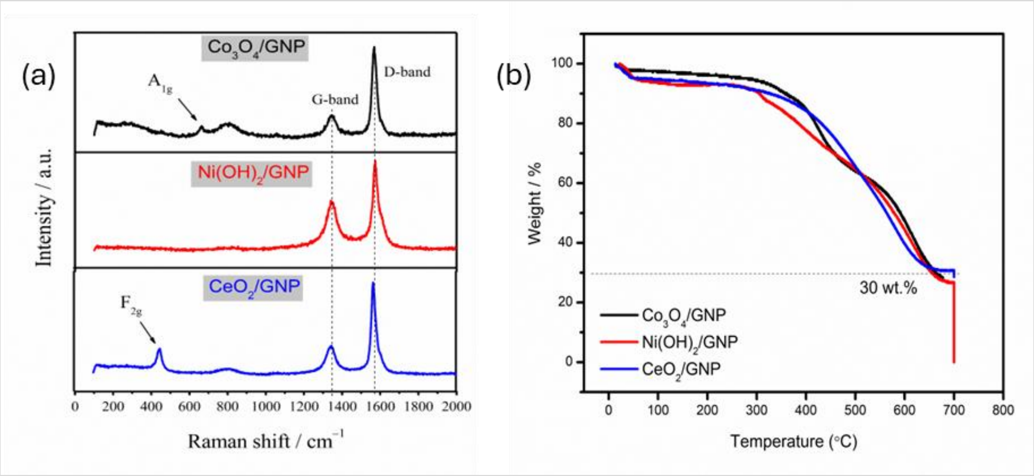

Figure 3A.3. (a) Raman spectra, and (b) TGA of Co_3O_4/GNP, $Ni(OH)_2$/GNP and CeO_2/GNP.

EDX (elemental mapping) is performed to confirm the incorporation of all the elements as expected in the prepared catalysts. These are presented in Figure 3A.4, 3A.5 and 3A.6. The atomic% composition of Ni, Co, Ce, O and C in the synthesized compounds are listed in the inset of these figures.

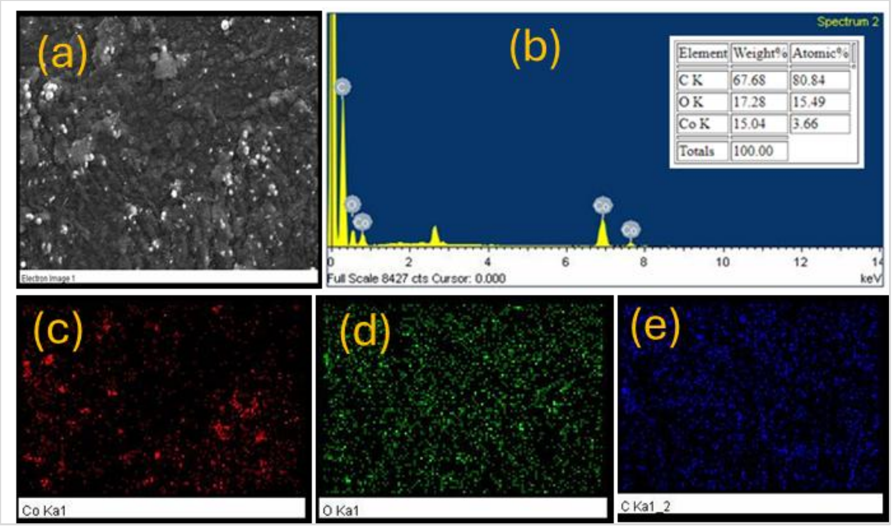

Element	Weight%	Atomic%
C K	67.68	80.84
O K	17.28	15.49
Co K	15.04	3.66
Totals	100.00	

Figure 3A.4. EDX analysis of Co_3O_4/GNP; (a) the electron image (b) the EDX pattern, and (c‒e) individual elemental maps for Co, O and C, respectively.

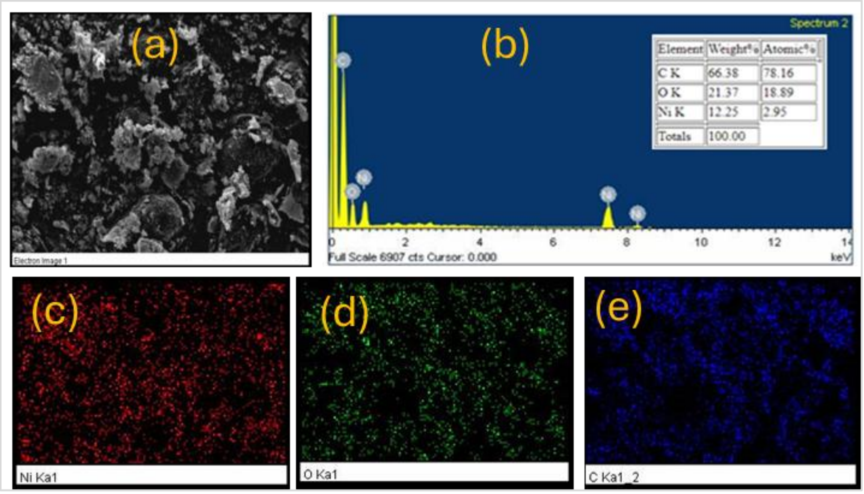

Element	Weight%	Atomic%
C K	66.38	78.16
O K	21.37	18.89
Ni K	12.25	2.95
Totals	100.00	

Figure 3A.5. EDX analysis of $Ni(OH)_2$/GNP; (a) the electron image (b) the EDX pattern, and (c–e) individual elemental maps for Ni, O and C, respectively.

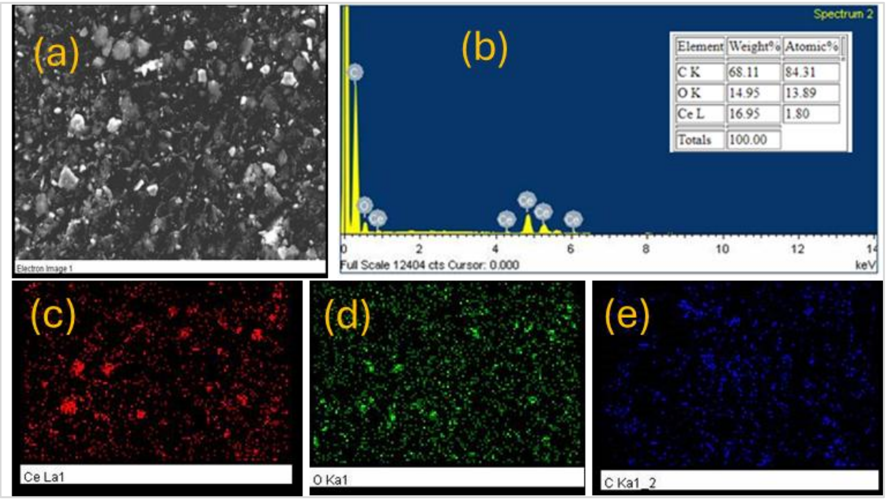

Element	Weight%	Atomic%
C K	68.11	84.31
O K	14.95	13.89
Ce L	16.95	1.80
Totals	100.00	

Figure 3A.6. EDX analysis of CeO_2/GNP; (a) the electron image (b) the EDX pattern, and (c–e) individual elemental maps for Ce, O and C, respectively.

3A.1.2 Electrocatalytic study

The electrocatalytic properties of the synthesized catalysts are evaluated towards ORR and OER by cyclic voltammetry (CV), linear sweep voltammetry (LSV), and chronoamperometry (CA) methods. The potential window taken for performing the ORR is 0.2 to −0.8 V and OER is 0.2 to 1.2 V. CV measurements were performed in N_2 and O_2 saturated 0.1M KOH (as supporting electrolytes) on a glassy carbon (GC) working electrode at a scan rate of 10 mVs^{-1} at room temperature. The counter electrode taken was a graphite rod. The ink suspension is prepared by mixing 5 mg of the powdered catalyst in 0.5 mL of de-ionised water, 2-Propanol and 0.5 wt.% Nafion solution. 3 μL of this suspension was dropcast on the GC-RDE to fabricate the WE. This makes a catalyst loading of 0.015 mg. The catalysts are cycled within the potential range of 0.2 to −0.8 V (vs. Hg/HgO) for ORR. All the potentials are presented with respect to reversible hydrogen electrode (RHE). The cyclic voltammograms of the as-synthesized catalysts as well as that of commercial 20 wt.% Pt/C and as purchased GNP are presented in Figure 3A.7.

All the catalysts display a sharp reductive current at ~0.8 V under O_2-saturated condition. This confirms that the materials are ORR active under the employed reaction conditions. Again, all the analysis were carried out using a rotating disc electrode (RDE). LSV measurements were performed using an RDE in O_2-saturated 0.1 M KOH at scan rate 10 mVs^{-1} at rotation speeds of 400, 900, 1600, 2500 and 3600 rpm. These are presented in Figure 3A.8.

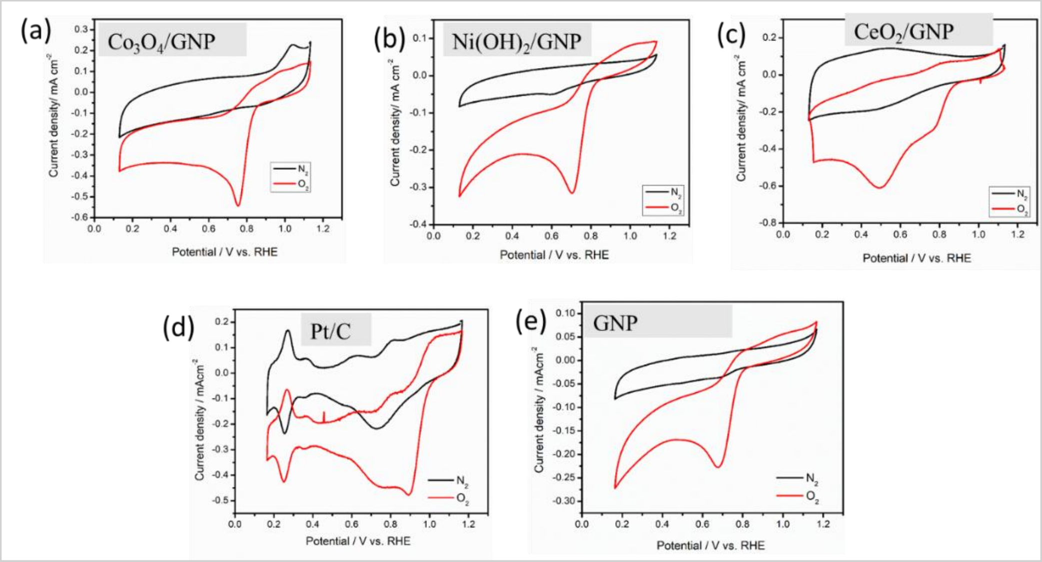

Figure 3A.7. CVs of (a) Co_3O_4/GNP, (b) $Ni(OH)_2$/GNP, (c) CeO_2/GNP, (d) commercial 20 wt% Pt/C, and (e) GNP in N_2- and O_2-saturated 0.1M KOH and scan rate 10 mV s^{-1}.

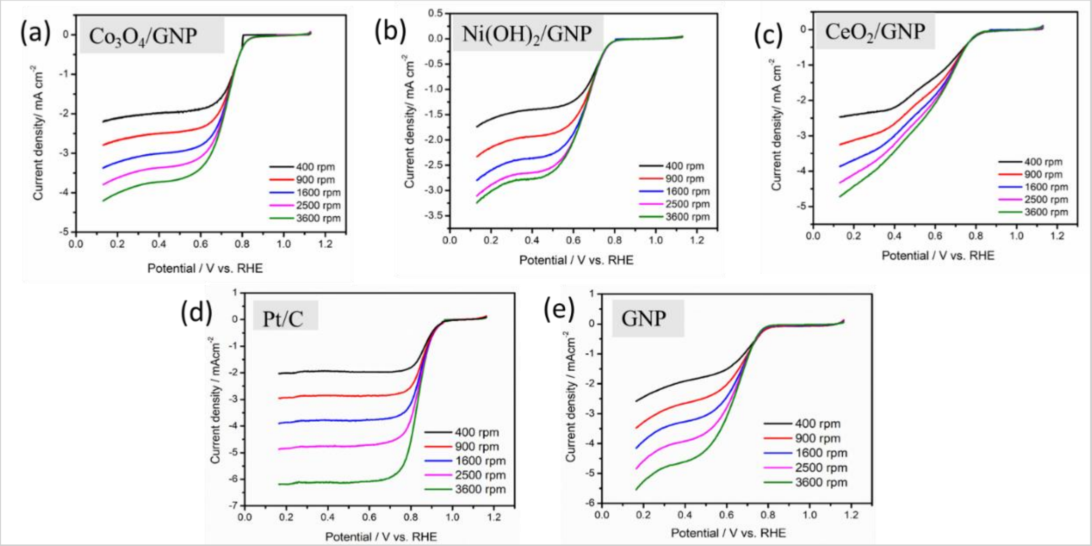

Figure 3A.8. LSVs of (a) Co_3O_4/GNP, (b) $Ni(OH)_2$/GNP, (c) CeO_2/GNP, (d) commercial 20 wt% Pt/C, and (e) GNP in O_2-saturated 0.1M KOH at different scan rates from 400–3600 rpm and scan rate 10 mV s^{-1}.

To compare their electroactivity towards ORR, an overlay of the LSVs at 1600 rpm for all the studied catalysts is presented in Figure 3A.9 (a). It is evident that Pt/C generates the highest current density as well as has the earliest onset potential ($E_{onset,ORR}$). All other important electrochemical parameters are listed in Table 3A.3. To get a fair comparison, we calculate the intrinsic activities (mass specific activities) of the catalysts. These are presented in a bar diagram in Figure 3A.9 (b). The current densities (j_m) at 0.5 V are normalized by the mass loading of the active element (30 wt.% for Co_3O_4/GNP, $Ni(OH)_2$/GNP and CeO_2/GNP, 20 wt.% Pt/C and 100% for GNP). The mass specific activities by calculated by normalizing the current densities at 0.5 V by the mass of the active element. The calculated parameters are listed below in Table 3A.1.

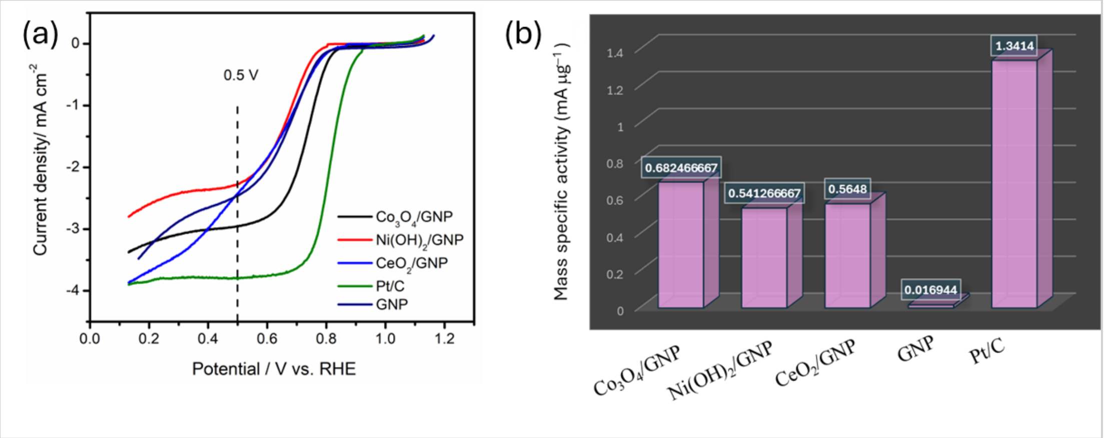

Figure 3A.9. (a) LSVs in O_2-saturated 0.1M KOH at 1600 rpm and scan rates 10 mV s^{-1}, and (b) Mass specific activities of the catalysts.

Table 3A.1. Details of calculation of mass specific activities*.

Catalyst	**J_m at 0.5 V (mA cm^{-2})**	**j_m (mA)**	**Catalyst load (mg)**	**active load (%)**	**active load (mg)**	**Sp. activity (mA µg^{-1})**
Co_3O_4/GNP	2.9	0.204	0.01	30%	0.0003	0.682
Ni(OH)$_2$/GNP	2.3	0.162	0.01	30%	0.0003	0.541
CeO$_2$/GNP	2.4	0.169	0.01	30%	0.0003	0.564
GNP	2.4	0.169	0.01	100%	0.01	0.016
Pt/C	3.8	0.268	0.01	20%	0.0002	1.341

* j_m is current density.

The ECSA is an important feature of electrified interfaces. This is the electrochemically accessible area of an electrode that facilitates charge transfer and storage [17]. It is derived from CVs at various scan rates shown in Figure 3A.10 (a–c) and the derived C_{DL} value is shown in Figure 3A.10 (d–e). The double layer capacitances (C_{DL})The method of calculating ECSA is already explained in Section 2.6.9. The calculated ECSAs are listed in Table 3A.3. It is seen that ECSA is the highest for CeO$_2$/GNP (70.4 m^2 g^{-1}), followed by Co_3O_4/GNP (24.5 m^2 g^{-1}) and then by Ni(OH)$_2$/GNP (14.5 m^2 g^{-1}).

Table 3A.2. List of parameters in ECSA calculation.

Catalyst	**C_{DL} / mF**	**Catalyst loading / g**	**ECSA / m^2 g^{-1}**
Co_3O_4/GNP	103	10^{-5}	24.5
$Ni(OH)_2$/GNP	66	10^{-5}	14.5
CeO_2/GNP	276	10^{-5}	70.4

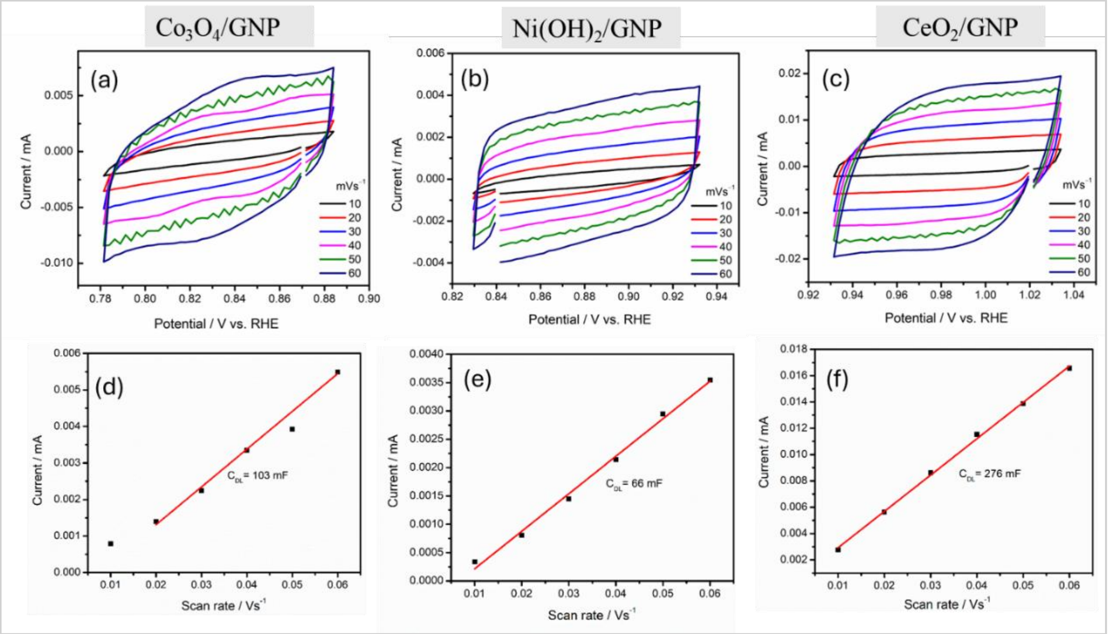

Figure 3A.10. (a–c) CVs of the as-synthesized catalysts at different scan rates from 10–60 mV s^{-1}, and (d–f) Double layer capacitance (C_{DL}) derived from slope of charging current vs. scan rates.

To understand further about the kinetics of the ORR processes for the as-synthesized catalysts, Koutecky-Levich (K-L) analyses are done as explained in Section 2.6.6 [18]. The K-L plots are shown in Figure 3A.11 (a─c). The lines display good linearity and parallelism. This affirms that the K-L assumptions hold good in the chosen window of 0.5─0.7 V. The number of electrons derived from the K-L slopes are presented in bar diagram of Figure 3A.11 (d). It is observed that at 0.5 V and 0.6 V, Co_3O_4/GNP proceeds via the favorable 4 e^- pathway while the other two catalysts $Ni(OH)_2$/GNP and CeO_2/GNP are far from 4 e^-.

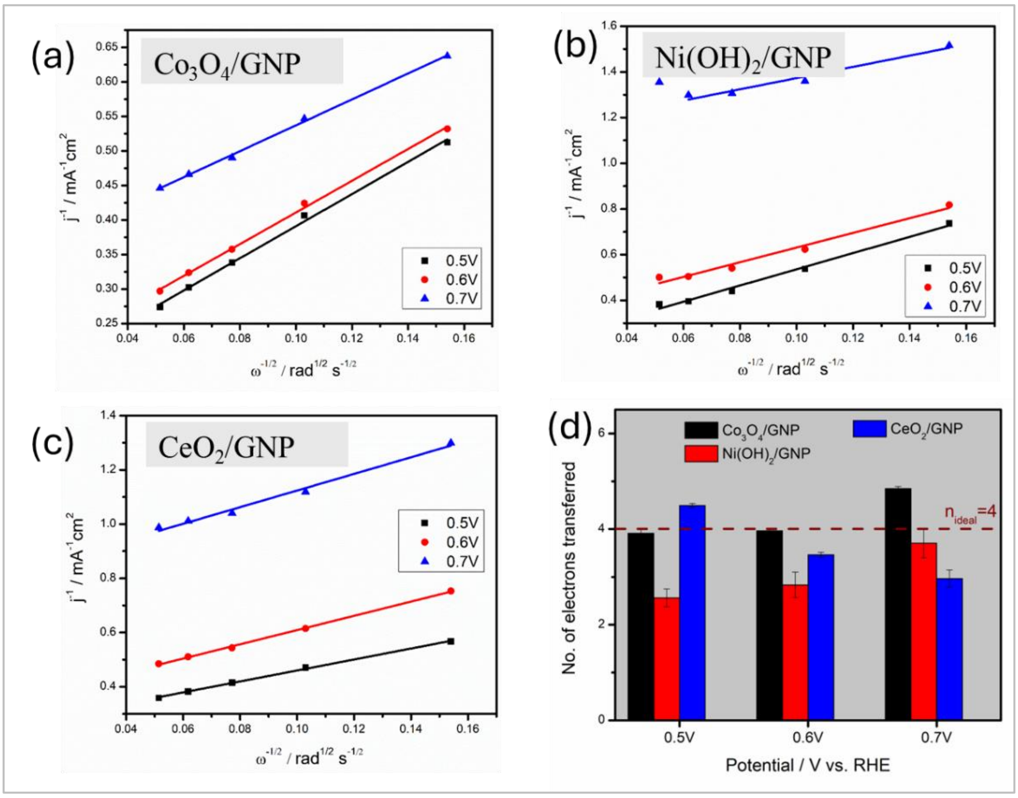

Figure 3A.11. (a–c) K-L plots of Co_3O_4/GNP, $Ni(OH)_2$/GNP and CeO_2/GNP at potentials 0.5 V, 0.6 V and 0.7 V, and (d) Bar diagram showing number of electrons (n) transferred in ORR process.

The stability and durability of the catalysts towards ORR are tested by ADT and CA tests. Figure 3A.12 presents the RDE-LSVs of the as-synthesized catalysts at 1600 rpm before and after 10,000 cycles. The potential windows for this are 0.43−0.93 V (for Co_3O_4/GNP) and 0.33−0.83 V (for $Ni(OH)_2$/GNP and CeO_2/GNP). This is chosen to accommodate the onset potential and plateau region. It is observed that has the least value, followed by and then by The $E_{1/2}$ (before and after ADT) and the shifts are presented in a bar diagram in Figure 3A.13. The shifts in $E_{1/2}$ follows the order: $Ni(OH)_2$/GNP (3 mV) < CeO_2/GNP (4 mV) < Co_3O_4/GNP = Pt/C (6 mv) indicating that $Ni(OH)_2$/GNP has the highest durability.

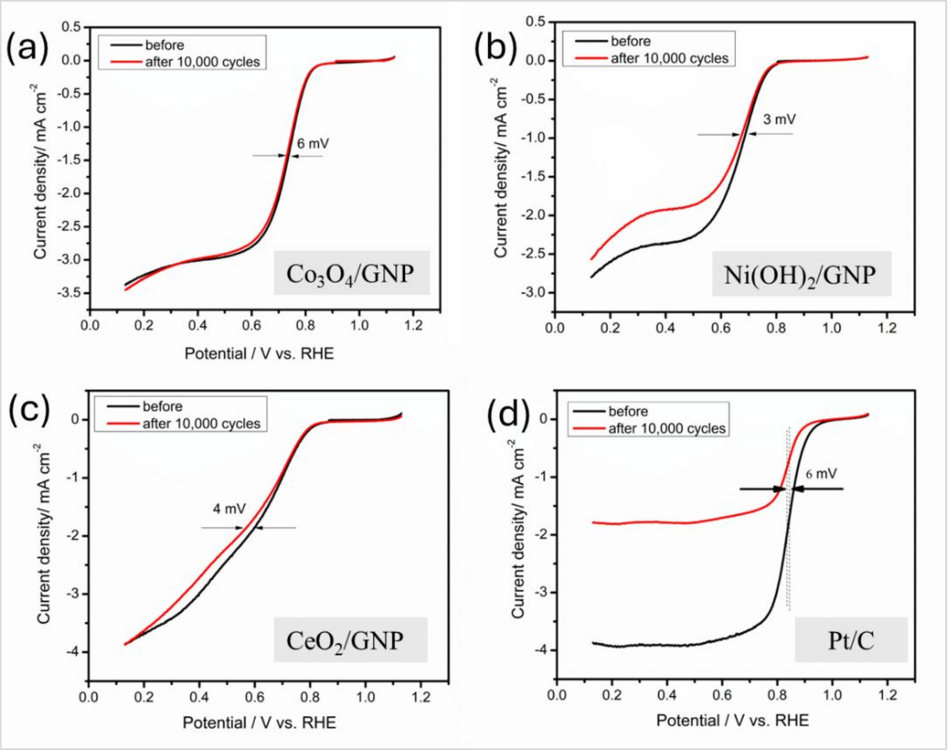

Figure 3A.12. LSVs at 1600 rpm of (a) Co_3O_4/GNP, (b) $Ni(OH)_2$/GNP, (c) CeO_2/GNP, and (d) commercial 20 wt.% Pt/C in O_2-saturated 0.1M KOH before and after 10,000 cycles.

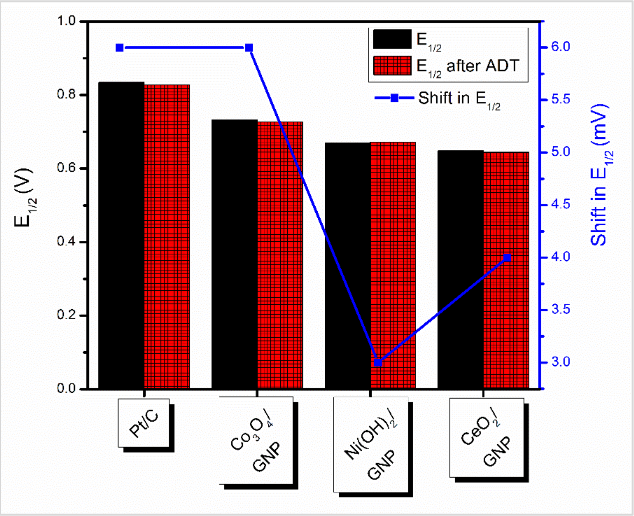

Figure 3A.13. Bar diagram showing $E_{1/2}$ before and after ADT (left axis) and their shifts in $E_{1/2}$ (right axis).

The CA test was performed under rotating condition of 1600 rpm and potential of 0.5 V. Figure 3A.14 shows the %retention of the initial currents at the end of 5.5 h.

$Ni(OH)_2$/GNP retains the highest current among them, followed by CeO_2/GNP and Co_3O_4/GNP.

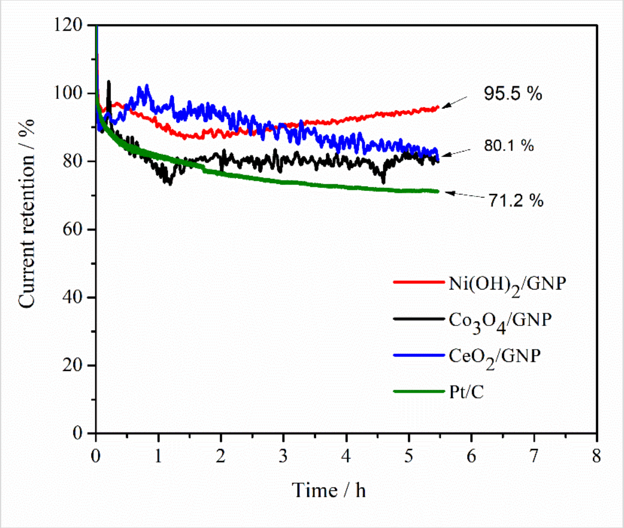

Figure 3A.14. CA test at 1600 rpm for the catalysts at 0.5V for 5.5 h.

The catalysts were tested for their OER affinity under N_2-saturated 0.1M KOH. This is shown in Figure 3A.15 (a). The Ej10 are marked and the calculated overpotential are presented in a bar diagram in Figure 3A.15 (b). It is observed that that $Ni(OH)_2$/GNP exhibits an overpotential only slightly higher than the commercial benchmark catalyst RuO_2.

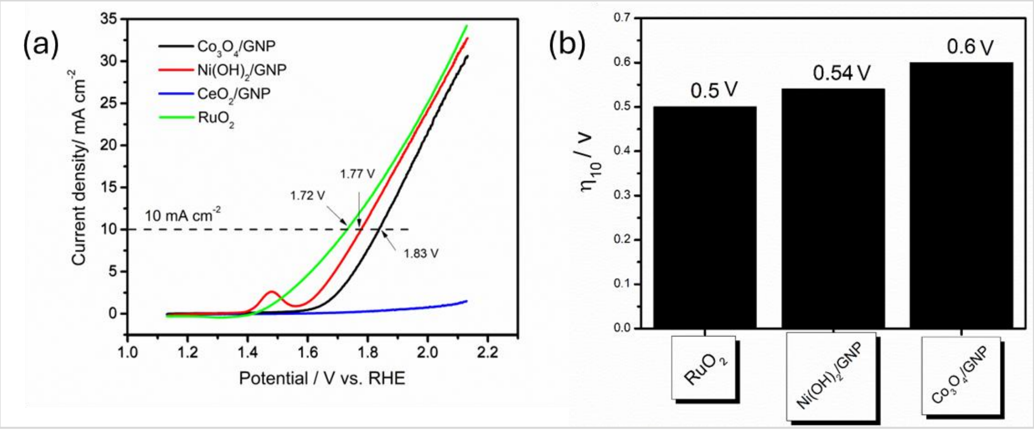

Figure 3A.15. (a) LSVs in N_2-saturated 0.1M KOH at 1600 rpm and scan rates 10 mV s^{-1}, and (b) Overpotentials of the catalysts for OER.

Table 3A.3. List of important electrocatalytic parameters- onset potential for ORR ($E_{onset,ORR}$), half wave potential ($E_{1/2}$), limiting current density (j_m), mass specific activity, ECSA, potential to reach 10 mA cm^{-2} of the catalysts towards ORR and ORR.

pElectrocatalyst	**$E_{onset,ORR}$ / V**	**$E_{1/2}$ / V**	**j_m / mA cm^{-2}**	**Sp. Activity / mA μg^{-1}**	**ECSA / m^2 g^{-1}**	**Ej10 / V**	**η_{10} /V**
Co_3O_4/GNP	0.85	0.733	–3.36	9.128	24.5	1.83	0.6
$Ni(OH)_2$/GNP	0.80	0.669	–2.79	7.239	14.5	1.77	0.54
CeO_2/GNP	0.83	0.648	–3.84	7.554	70.39	Did not achieve j10	–
Pt/C	0.96	0.834	–3.91	17.941	–	–	
RuO_2	–	–	–	–	–	1.72	0.5

3A.2 Conclusions

In summary, three non-PGM based catalysts, viz. Co_3O_4/GNP, $Ni(OH)_2$/GNP and CeO_2/GNP are prepared via simple solvothermal process. The synthesized catalysts are bifunctional towards ORR and OER. Among them, Co_3O_4/GNP exhibit preferred electrocatalytic parameters like most positive $E_{1/2}$ and proceeds via the favorable 4 e$^-$ pathway. From this observation, we understand that cobalt-based mixed electrocatalysts are to be studied thoroughly in the following chapters. $Ni(OH)_2$/GNP exhibits the highest stability and durability, even surpassing Pt/C which indicates that it could be a potential candidate to study. Because the ECSA was seen to be the highest for CeO_2/C, it can be utilized as catalytic activity booster with Co_3O_4/GNP and $Ni(OH)_2$/GNP. From this section, we conclude with the note that Co_3O_4/CeO_2/GNP, $Ni(OH)_2$/CeO_2/GNP and Co_3O_4/ Ni(OH)2/CeO_2/GNP can be explored for better understanding of the role of interfaces between the component oxides.

Section 3B: Tuning the electrocatalytic activity of the bimetallic (hydro)oxides of Co_3O_4 and $Ni(OH)_2$ by integration of CeO_2

In this section, we synthesize three mixed (hydro)oxides, viz. Co_3O_4/CeO_2/GNP, $Ni(OH)_2/CeO_2$/GNP and $Co_3O_4/Ni(OH)_2/CeO_2$/GNP (shortly denoted as CoNiCe/GNP). These are tested for electrocatalytic ORR and OER. The synthesis procedure is mentioned in Section 2.2.4, 2.2.5 and 2.2.6 respectively.

3B.1 Results and discussion

3B.1.1 Physical characterization

The PXRD spectra obtained for the as-synthesized catalysts and the standard JCPDS reference peaks are presented in Figure 3B.1.

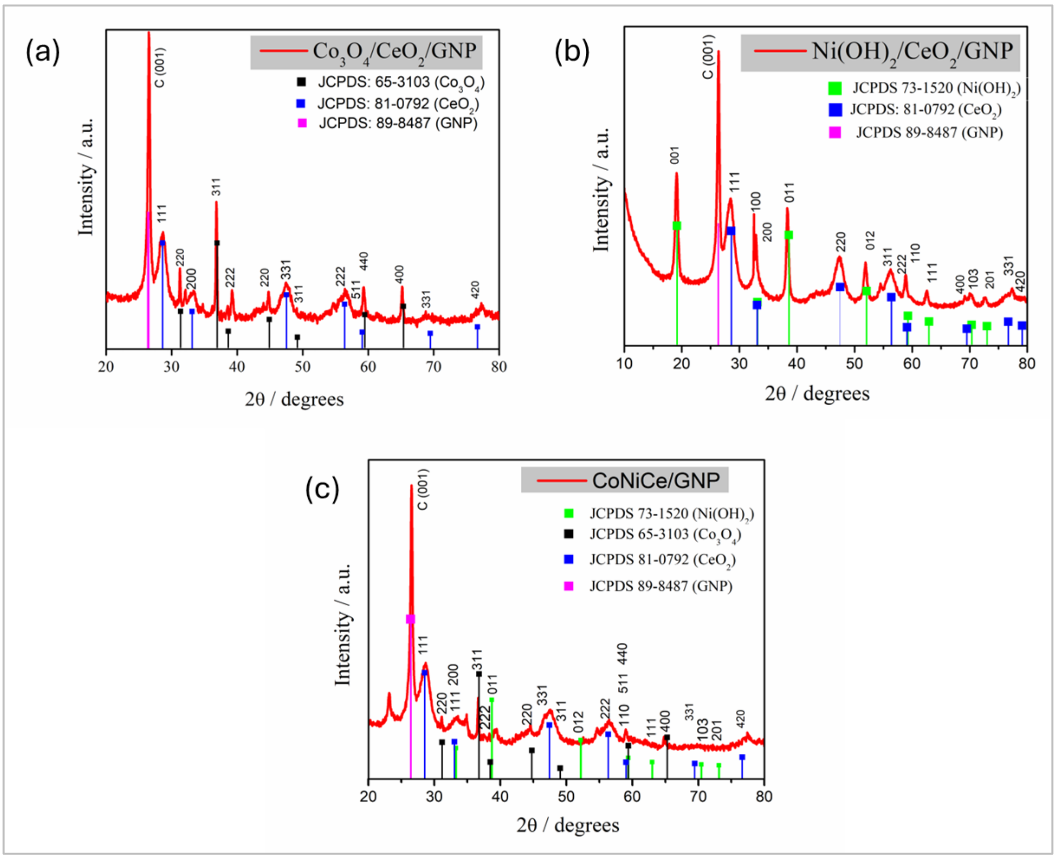

Figure 3B.1. PXRD of (a) Co_3O_4/CeO_2/GNP, (b) $Ni(OH)_2/CeO_2$/GNP, and (c) CoNiCe/GNP.

Each of them has the (100) plane of GNP at 2θ=26.5° (JCPDS # 89-8487). The diffraction pattern of Co_3O_4/CeO_2/GNP matches well with JCPDS# 65-3103 and JCPDS# 81-0792. Similarly, the diffraction pattern of $Ni(OH)_2$/CeO_2/GNP matches well with JCPDS# 73-1520 and JCPDS# 81-0792. And that of NiCoCe/GNP matches well with each of the above-mentioned JCPDS card numbers. This reveals that these are mixed metal (hydr)oxides consisting of oxides/hydroxides interfaces. Unlike that in Section 3A, the diffraction patterns of these CeO_2 mediated (hydr)oxides are amorphous in nature with broad peaks. The FTIR spectra of the catalysts are presented in Figure 3B.2. Similar to Section 3A, broad bands for O─H stretching (~3500 cm^{-1}), O─H bending (~1633 cm^{-1}) and C─H stretching (symmetric and asymmetric; at ~2920, 2856 cm−1) bands are observed [5,9–11]. In Figure 3B.2 (a) the FT-IR spectrum exhibited a peak at ~ 656 cm^{-1} that represents M–O–M stretching and one at ~ 570 cm^{-1} for M=O [9]. In Figure 3B.2 (b), a slight shifting in M─O bond to higher wavenumber is observed at ~520 cm^{-1} than the original Ni─O and Ce─O bond. In Figure 3B.2 (c) the characteristic peaks of Ni, Co and Ce are masked by the overlap of bands.

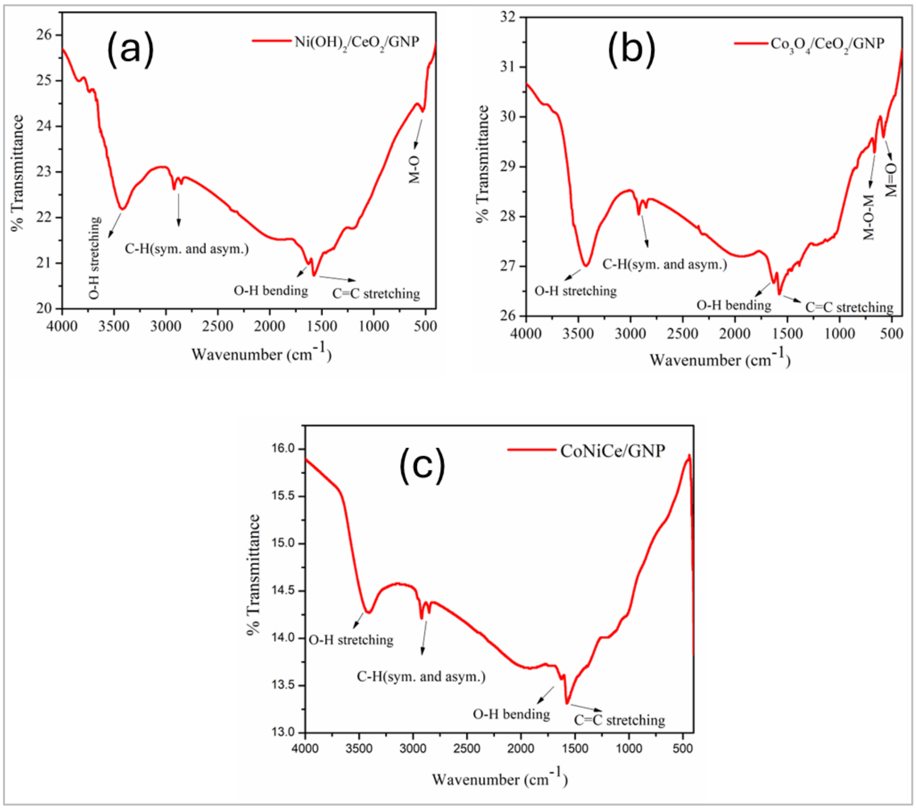

Figure 3B.2. FTIR spectra of (a) $Ni(OH)_2$/CeO_2/GNP, (b) Co_3O_4/CeO_2/GNP, and (c) CoNiCe/GNP.

Similar to Section 3A, the Raman spectra of the materials (see Figure 3B.3 (a)) reveal an intense G-band (at ~1350 cm^{-1}) and D-band (at ~1570 cm^{-1}) [12]. Apart from this, other Raman active vibrational modes, viz. F_{2g} (CeO_2) and A_{1g} (Co_3O_4) are also observed [13–16]. However, the F_{2g} mode of Ce–O is the most intense in the hybrid Co_3O_4/CeO_2/GNP. The mass loading of the active metal oxides and hydroxides were confirmed from TGA (in air) analysis shown in Figure 3B.3 (b). There is a weight loss of 70% which confirms that the active mass is 30 wt.%. The 70 wt.% of carbon content or GNP is air-oxidized as CO_2.

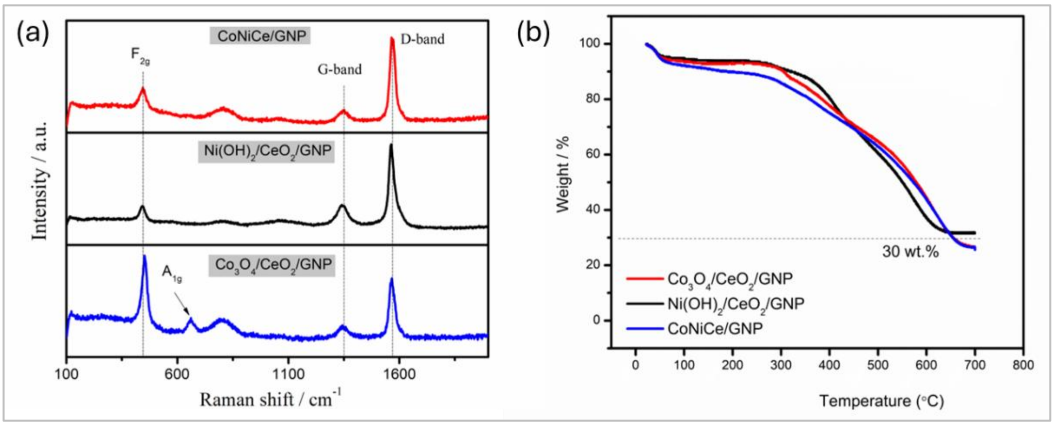

Figure 3B.3. (a) Raman spectra, and (b) TGA of the as-synthesized catalysts.

EDX (elemental mapping) is performed to confirm the incorporation of all the elements in the prepared catalysts. These are presented in Figure 3B.4, 3B.5 and 3B.6. The atomic% composition of Ni, Co, Ce, O and C in these hybrid composites are listed in the insets. From inset of Figure 3B.4 (b), the atomic ratio of Co : Ce = 3:1 in Co_3O_4/CeO_2/GNP. From Figure 3B.5 (b), Ni : Ce = 3:1 in $Ni(OH)_2/CeO_2$/GNP and from Figure 3B.6 (b), Co,Ni : Ce = 3:1.

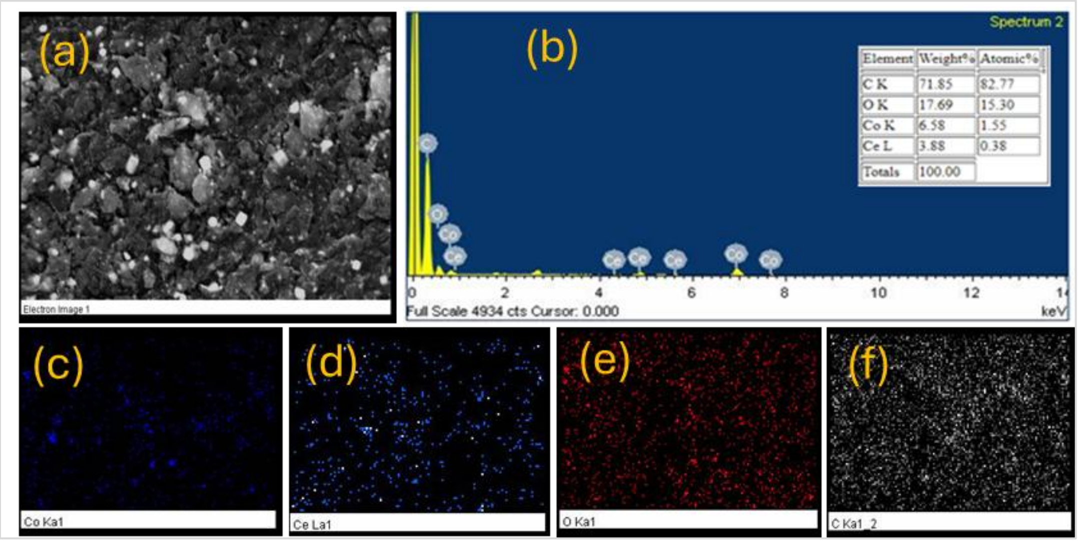

Element	Weight%	Atomic%
C K	71.85	82.77
O K	17.69	15.30
Co K	6.58	1.55
Ce L	3.88	0.38
Totals	100.00	

Figure 3B.4. EDX analysis of Co_3O_4/CeO_2/GNP; (a) the electron image, (b) the EDX pattern, and (c–f) individual elemental maps for individual Co, Ce, O and C, respectively.

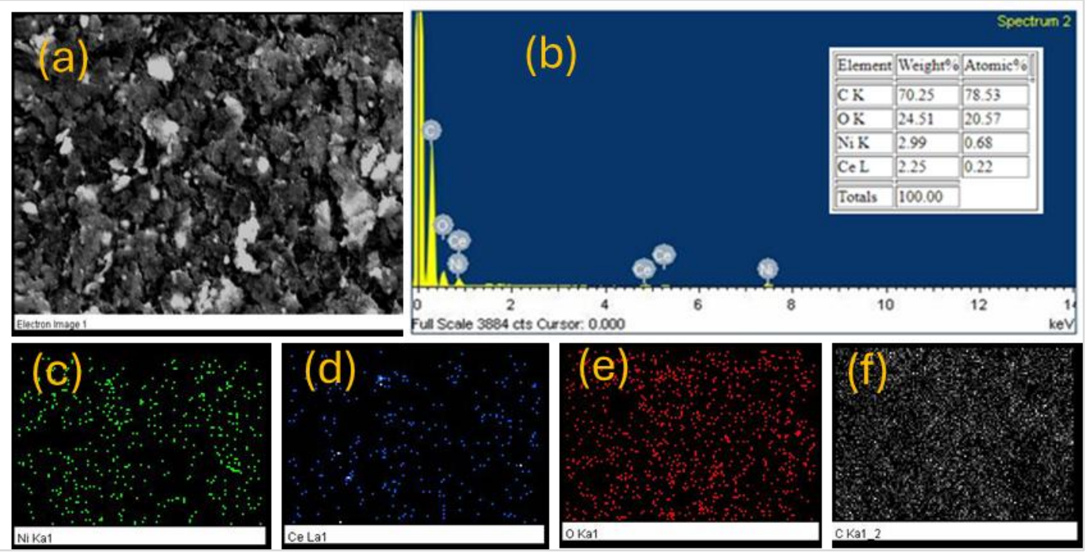

Element	Weight%	Atomic%
C K	70.25	78.53
O K	24.51	20.57
Ni K	2.99	0.68
Ce L	2.25	0.22
Totals	100.00	

Figure 3B.5. EDX analysis of $Ni(OH)_2/CeO_2$/GNP; (a) the electron image, (b) the EDX pattern, and (c–f) individual elemental maps for individual Ni, Ce, O and C, respectively.

.

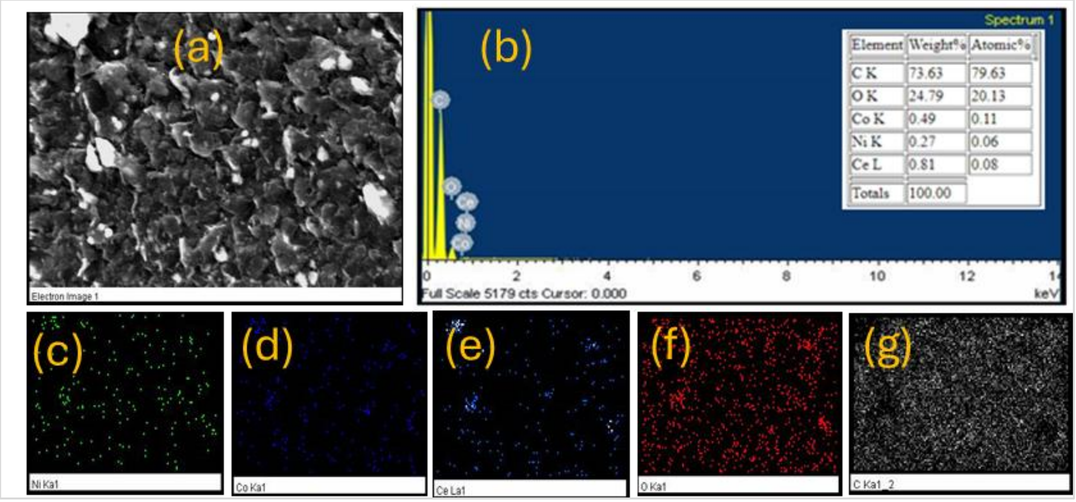

Element	Weight%	Atomic%
C K	73.63	79.63
O K	24.79	20.13
Co K	0.49	0.11
Ni K	0.27	0.06
Ce L	0.81	0.08
Totals	100.00	

Figure 3B.6. EDX analysis of CoNiCe/GNP; (a) the electron image, (b) the EDX pattern, and (c–g) individual elemental maps for individual Ni, Co, Ce, O and C, respectively.

Structure and morphology of the as-synthesized materials are studied TEM and HRTEM images presented in Figure 3B.7, 3B.8 and 3B.9.

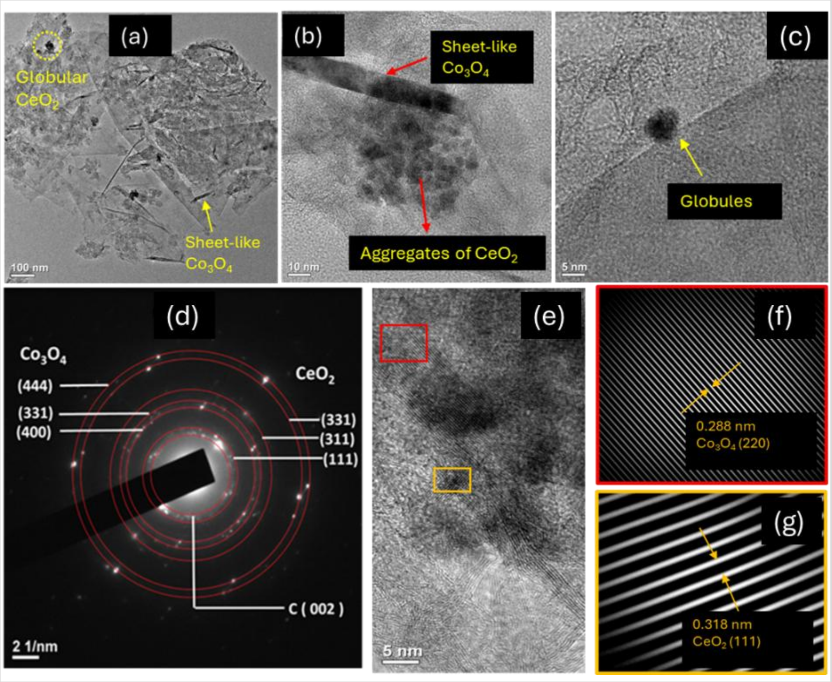

Figure 3B.7. (a,b,c) Low-resolution TEM images, (d) SAED pattern, (e) high-resolution TEM (HRTEM) image, and (f– g) FFT images of the marked regions in (e) of Co_3O_4/CeO_2/GNP.

The interplanar distances (d-spacing) are calculated by processing the observed lattice fringes from HRTEM images in ImageJ software [19]. From the low-resolution TEM images shown in Figure 3B.7 (a,b,c), 3B.8 (a,b) and 3B.9 (a), it is seen that Co_3O_4 and $Ni(OH)_2$ have sheet-like structures while CeO_2 is mostly globular aggregates. Such sheet-like structures are consistent with previously reported literature [20–22]. SAED patterns shown in Figure 3B.7 (d) and 3B.9 (c) show dotted concentric rings indicating polycrystalline nature of Co_3O_4/CeO_2/GNP and CoNiCe/GNP. Figure 3B.8 (c,d) shows presence of both dotted rings and diffused rings indicating absence of both long-range and short-range order.

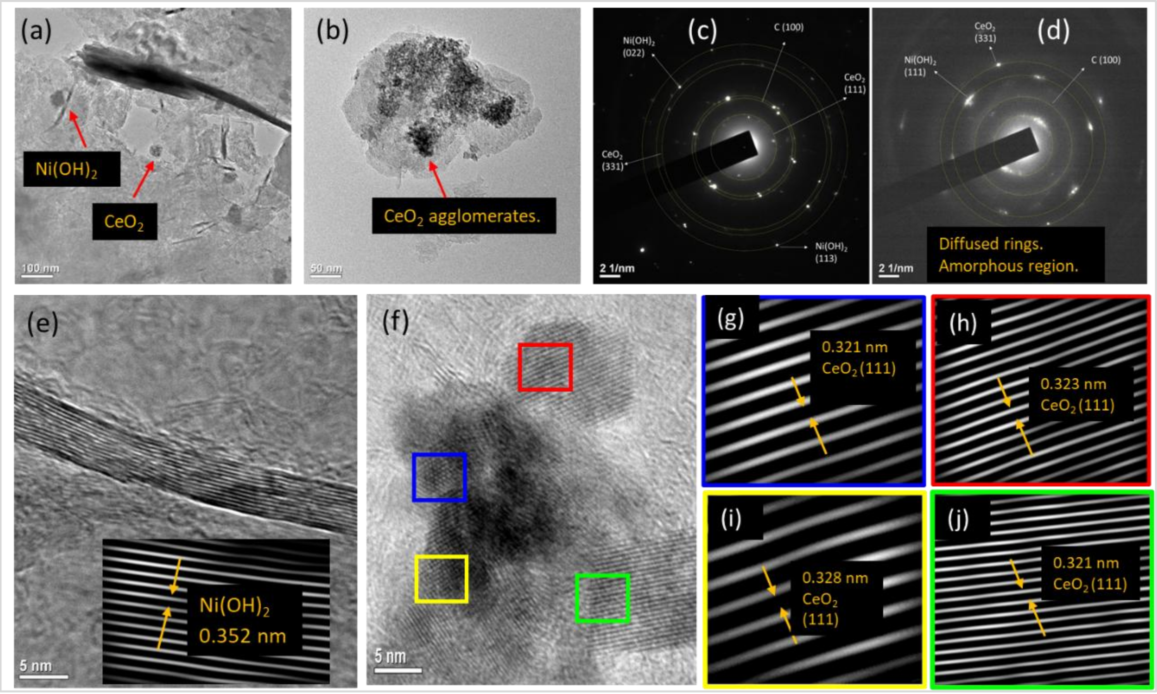

Figure 3B.8. (a,b) Low-resolution TEM images, (c,d) SAED patterns, (e,f) high-resolution TEM (HRTEM) images, and (g– j) FFT images of the marked regions in (f) of $Ni(OH)_2/CeO_2$/GNP.

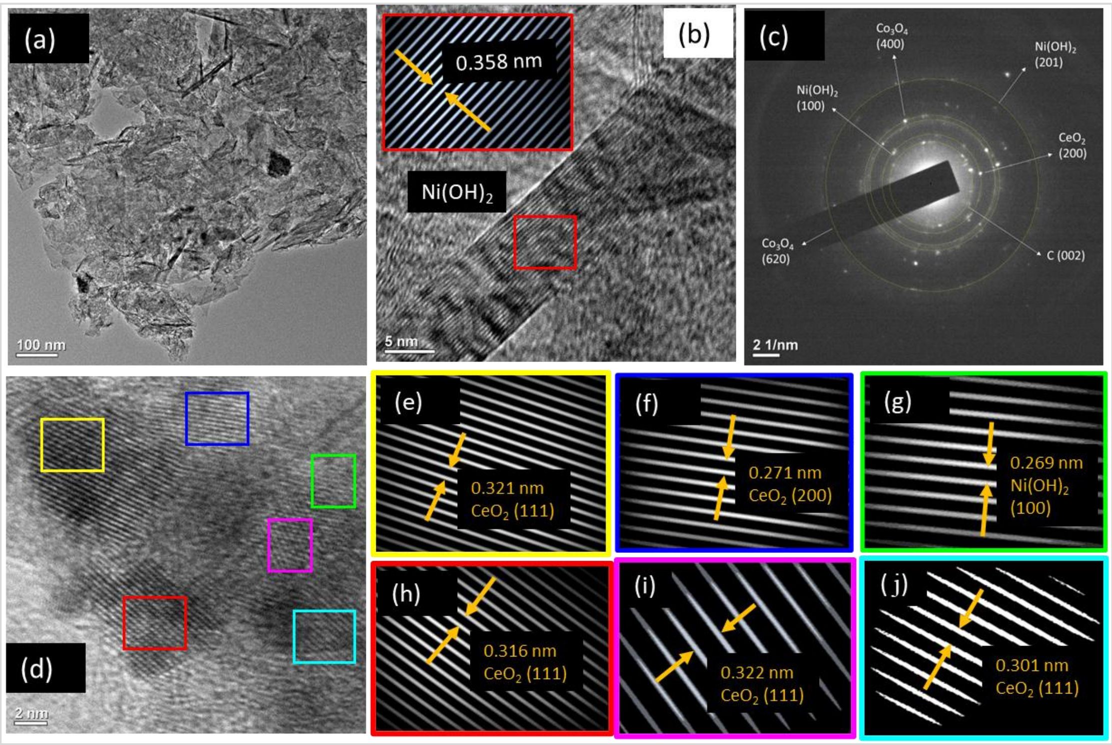

Figure 3B.9. (a) Low-resolution TEM images, (b) high-resolution TEM (HRTEM) image (c), SAED pattern, (d) HRTEM image at a different resolution, and (e‒j) FFT images of the marked regions in (d) of CoNiCe/GNP. From the FFT images, most observed fringes are crystallites of CeO_2 while the other components, viz. $Ni(OH)_2$, Co_3O_4 and CeO_2 are amorphous.

3B.1.2 Electrocatalytic study

The ink composition, potential window and WE, RE and CE are same as mentioned in Section 3A. The CVs and RDE-LSVs at different rotations are shown in Figure 3B.10. All the materials are electroactive towards ORR. For comparison, Figure 3B.11 (a) presents the LSVs of the catalysts at 1600 rpm. From this, the current densities at 0.4 V are normalized by the mass loading of the active element (30 wt.% for Co_3O_4/CeO_2/GNP, $Ni(OH)_2/CeO_2$/GNP, CoNiCe/GNP and 20 wt.% Pt/C). The calculated mass specific activities are presented in a bar diagram in Figure 3B.11 (b). It is seen that specific mass activity follows the order: Pt/C > Co_3O_4/CeO_2/GNP > CoNiCe/GNP > $Ni(OH)_2/CeO_2$/GNP.

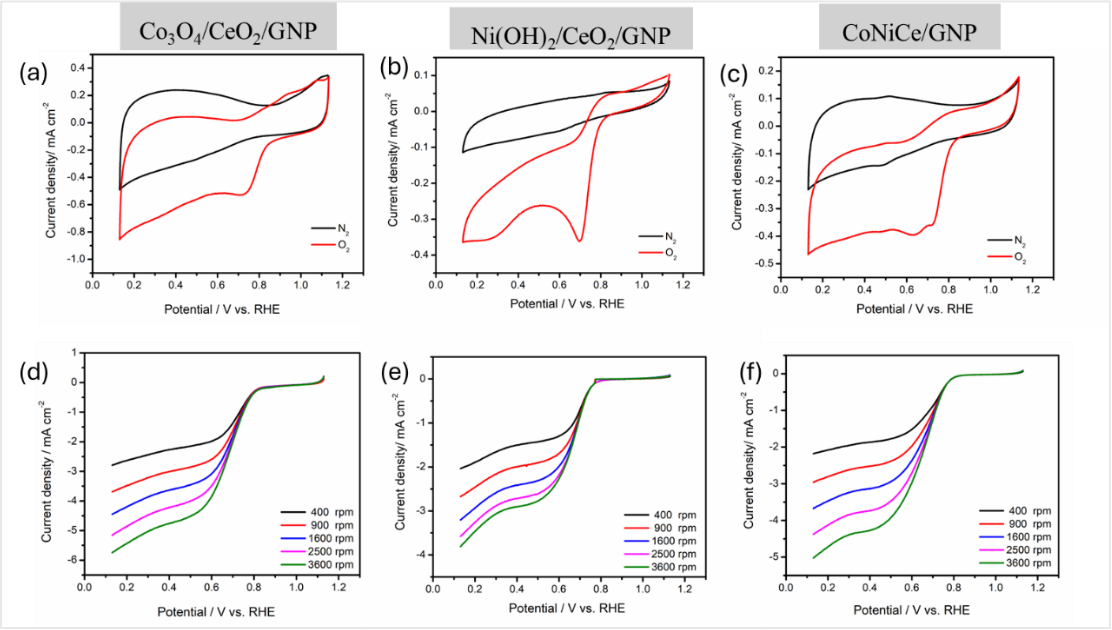

Figure 3B.10. (a–c) CVs of $Co_3O_4/CeO_2/GNP$ (a), $Ni(OH)_2/CeO_2/GNP$ (b), and CoNiCe/GNP (c) in N_2- and O_2-saturated) in 0.1M KOH , and (d–e) LSVs of $Co_3O_4/CeO_2/GNP$ (d), $Ni(OH)_2/CeO_2/GNP$ (e), and CoNiCe/GNP (f) at different rotation rates from 400–3600 rpm.

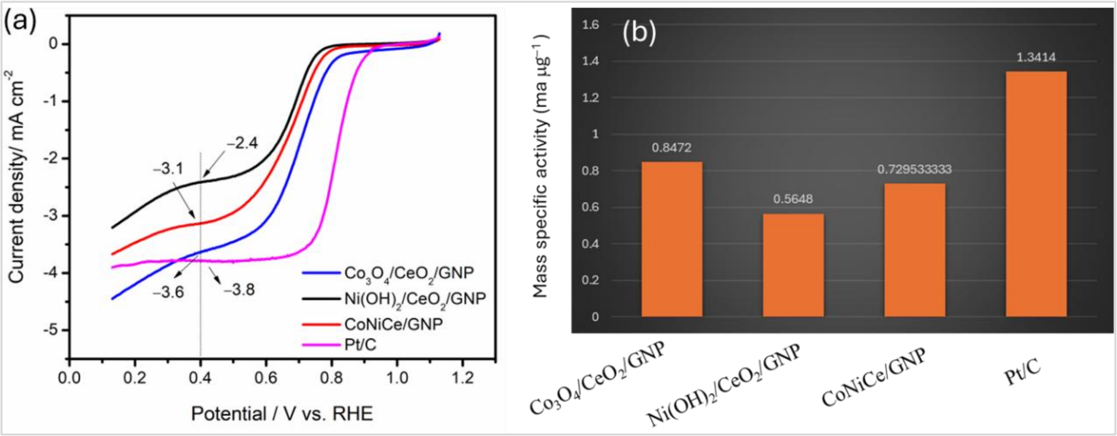

Figure 3B.11. (a) LSV@1600 rpm for ORR, and (b) Bar diagram representing mass specific activities calculated at 0.4 V.

Table 3B.1 Details of calculation of mass specific activities.

Catalyst	J_m at 0.4 V (mA cm^{-2})	j_m (mA)	Load (mg)	active load (%)	active load (mg)	Sp activity (mA μg^{-1})
Co_3O_4/CeO_2/GNP	3.6	0.254	0.01	30%	0.0003	0.847
$Ni(OH)_2/CeO_2$/GNP	2.4	0.169	0.01	30%	0.0003	0.564
CoNiCe/GNP	3.1	0.218	0.01	30%	0.0003	0.729
Pt/C	3.8	0.268	0.01	20%	0.0002	1.341

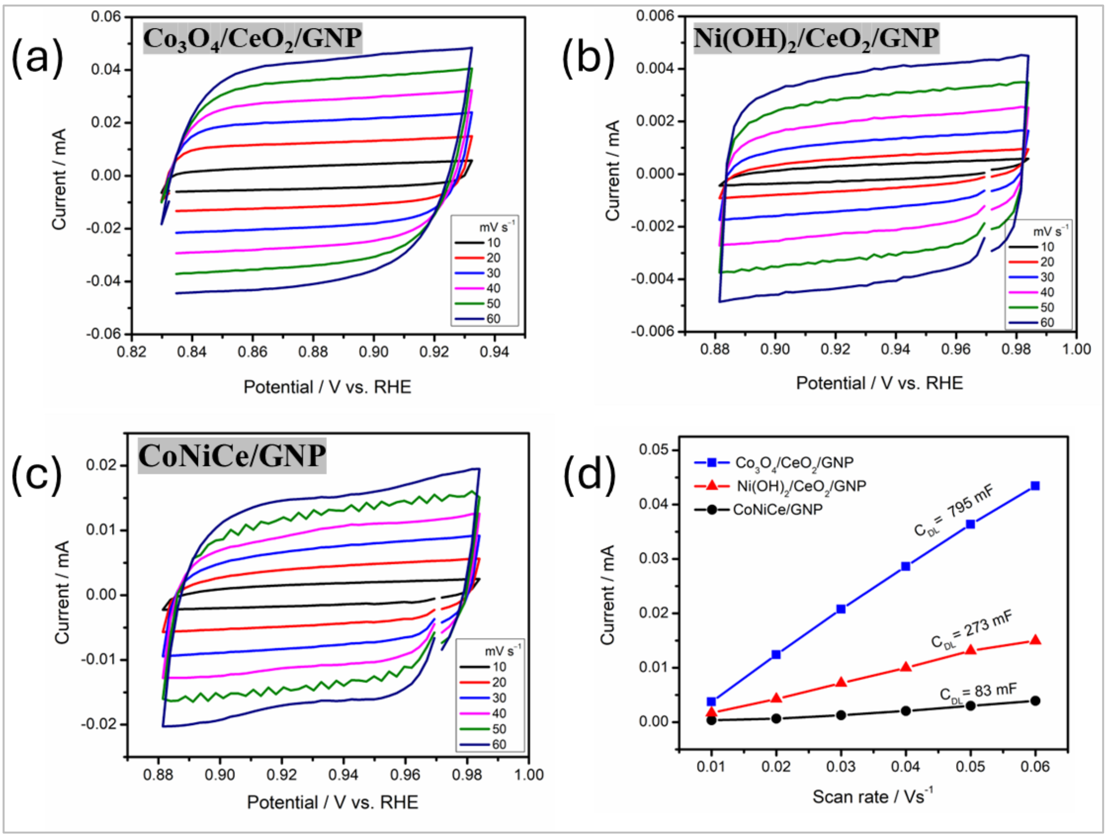

Figure 3B.12. (a–c) CVs of the catalysts at different scan rates, and (d) Double layer capacitance (C_{DL}) derived from slope of charging current of the CVs.

To correlate the intrinsic activities, we calculate the mass specific ECSAs from scan-rate dependent CVs shown in Figure 3B.12 (a–c). The derived C_{DL} values are shown in Figure 3B.12 (d). This is then employed in calculating the mass specific ECSAs according to the equation mentioned in Section 2.6.9. The calculated mass specific ECSAs are presented in a bar diagram in Figure 3B.13 where the same trend was observed: Co_3O_4/CeO_2/GNP > CoNiCe/GNP > $Ni(OH)_2/CeO_2$/GNP. This implies that Co_3O_4/CeO_2/GNP has the highest number of accessible electroactive sites.

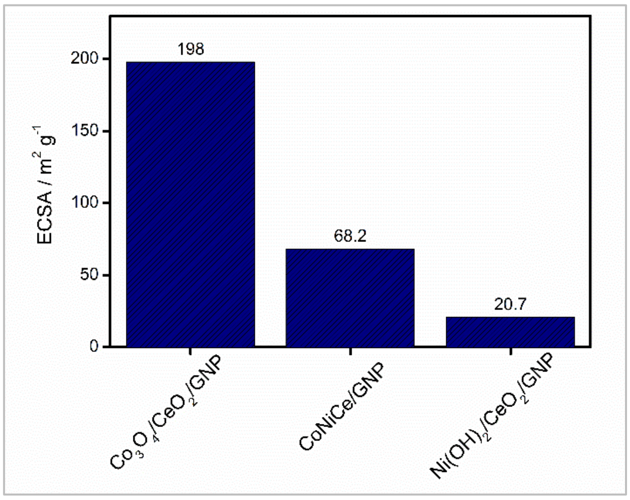

Figure 3B.13. Bar diagram representing mass specific ECSAs.

To gain insights on the kinetics, we have the Koutecky-Levich (K-L) plots in 0.5−0.7 V shown in Figure 3B.14 (a−c). Good parallelism and linearity is observed which indicates that these are catalysts have sluggish kinetics [23]. The derived number of electrons (n) participating in ORR as calculated from K-L equation are presented in the bar diagram in Figure 3B.14 (d). The catalyst Co_3O_4/CeO_2/GNP occurs via the most favorable direct 4 e^- pathway while the 'n' values for $Ni(OH)_2/CeO_2$/GNP and CoNiCe/GNP are far from '4'.

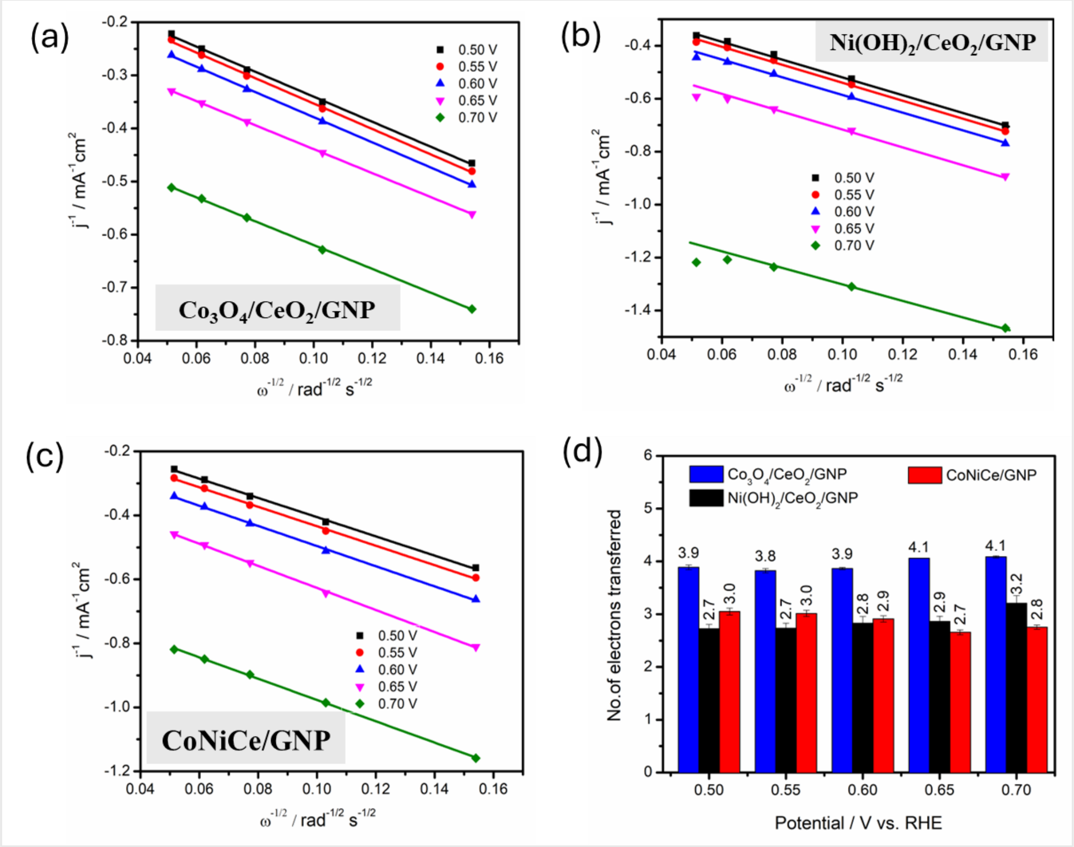

Figure 3B.14. (a– c) K-L plots of Co_3O_4/CeO_2/GNP (a), $Ni(OH)_2/CeO_2$/GNP (b), CoNiCe/GNP (c) in the potential window 0.5–0.7 V, and (d) Bar diagram representing number of electrons transferred ‘n’ during ORR.

For practical utility and commercialization, stability and stress-resistant nature is one of the primary requirements. The commercial benchmark 20 wt.% Pt/C catalyst suffers from low longevity due to metal poisoning and agglomeration [24]. The as-synthesized catalysts are tested for stability by ADT and CA. These tests are explained in detail in Section 2.6.7 and 2.6.8. Figure 3B.15 shows the ADT results after 10,000 potential cycles of CV along with the shifts in their half-wave potentials ($E_{1/2}$). Here, the $E_{1/2}$ values are the potentials at half-height of the limiting current at 0.4 V. A lower value of the shift ($\Delta E_{1/2}$) indicates greater tolerance and durability. Co_3O_4/CeO_2/GNP exhibits the least value (4mV), even lesser than commercial Pt/C.

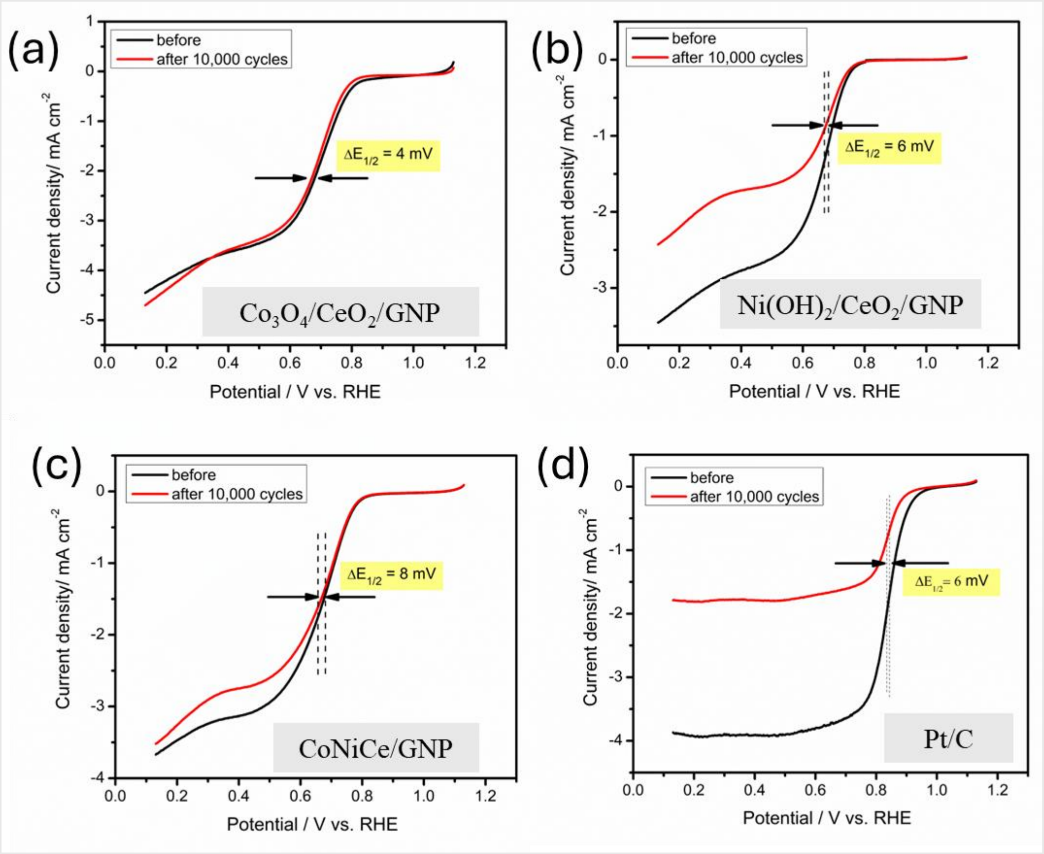

Figure 3B.15. ADT of (a) Co_3O_4/CeO_2/GNP, (b) $Ni(OH)_2/CeO_2$/GNP, (c) CoNiCe/GNP, and (d) 20 wt.% Pt/C.

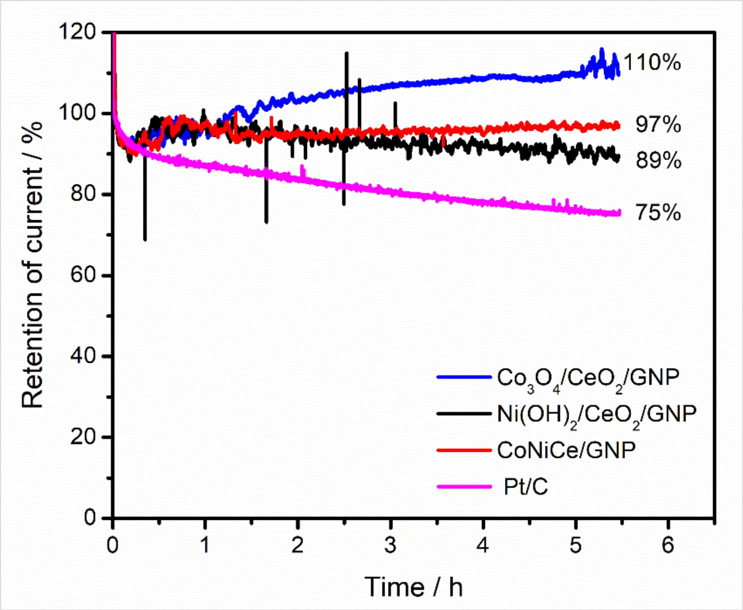

Figure 3B.16. CA test at 0.5 V of the as-synthesized catalysts and commercial 20 wt.% Pt/C.

CA test for 5.5 h reveals that all the as-synthesized catalysts retain higher currents than the commercial Pt/C. It is seen from Figure 3B.16 that the %retention of initial currents are in the order: Co_3O_4/CeO_2/GNP > CoNiCe/GNP > $Ni(OH)_2/CeO_2$/GNP > Pt/C. However, it is to be noted that Co_3O_4/CeO_2/GNP exhibits 110% retention. This can be attributed to in-situ surface reconstruction of the catalyst. More information on this can be obtained by performing operando experiments.

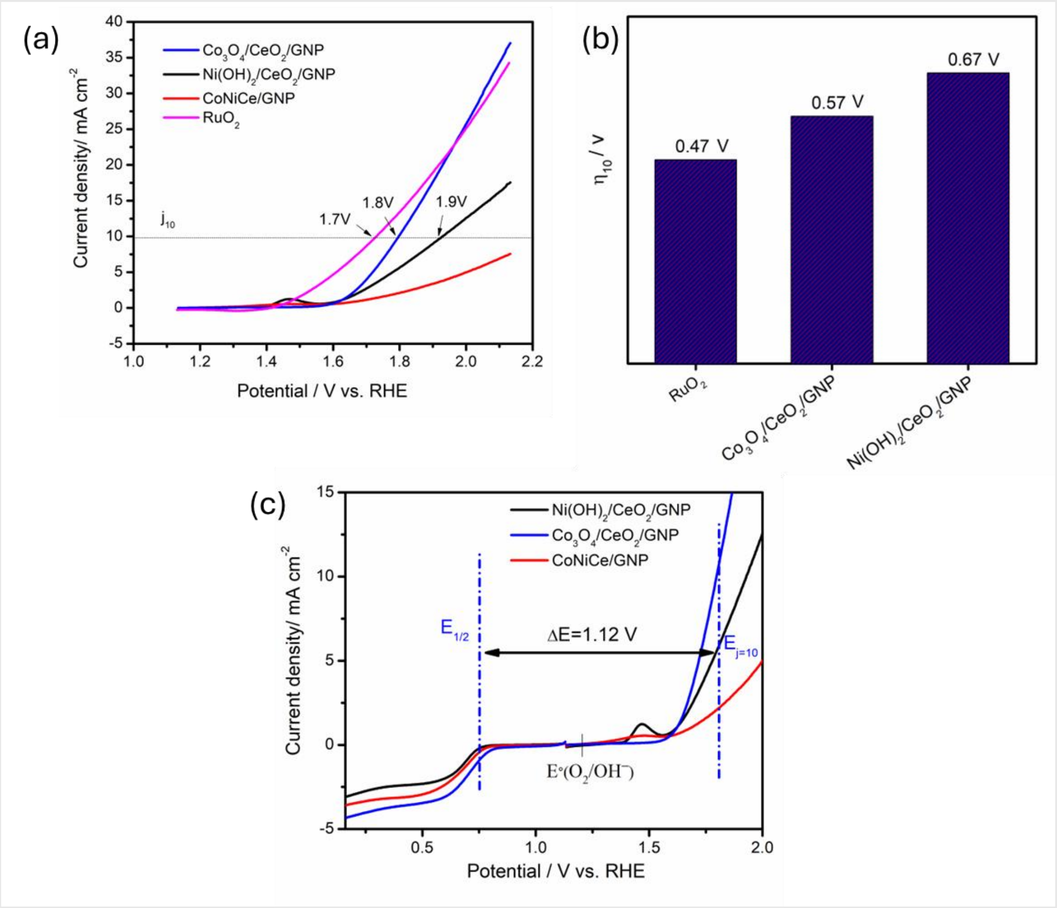

Figure 3B.17. (a) LSV@1600 rpm for OER, (b) Bar diagram representing overpotentials, and (c) Diagram showing bifunctionality index of Co_3O_4/CeO_2/GNP.

To check the bifunctionality of the catalysts, we perform OER in N_2-saturated 0.1M KOH at 1600 rpm (Figure 3B.17 (a)) and compare their overpotentials by employing the formula mentioned in Section 2.6.10. The calculated overpotentials (η10) are presented in a bar diagram in Figure 3B.17 (b). Co_3O_4/CeO_2/GNP exhibits the lowest overpotential among the as-synthesized catalysts and it follows the order: RuO_2 > Co_3O_4/CeO_2/GNP > $Ni(OH)_2/CeO_2$/GNP > CoNiCe/GNP. However, the overpotentials are not very impressive in comparison to the commercial benchmark RuO_2. The potential gap between ORR and OER or the bifunctionality index (ΔE) is calculated to be the least for Co_3O_4/CeO_2/GNP and is shown in Figure 3B.17 (c). The potentials required by the catalysts to attain the standard 10 mA cm^{-2} mark (denoted as E(j10)) are listed in Table 3B.2.

Table 3B.2. List of important electrocatalytic parameters- onset potential for ORR ($E_{onset,ORR}$), half wave potential ($E_{1/2}$), limiting current density (j_m), mass specific activity, ECSA, potential to reach 10 mA cm^{-2} of the catalysts towards ORR and ORR.

Electrocatalyst	**$E_{onset,ORR}$ / V**	**$E_{1/2}$ / V**	**j_m / mA cm^{-2}**	**Sp. Activity / mA μg^{-1}**	**ECSA / m^2 g^{-1}**	**Ej10 / V**	**η_{10} /V**
Co_3O_4/CeO_2/GNP	0.86	0.73	–3.6	0.564	198	1.8	0.57
$Ni(OH)_2/CeO_2$/GNP	0.82	0.66	–2.4	0.376	20.7	1.9	0.67
CoNiCe/GNP	0.83	0.66	–3.1	0.486	68.2	Did not achieve j10	–
Pt/C	0.96	0.834	–3.8	0.894	–	–	–
RuO_2	–	–	–	–	–	1.72	0.47

3B.2 Conclusions

In summary, we have synthesized three non-PGM ceria-based catalysts, viz. Co_3O_4/CeO_2/GNP, $Ni(OH)_2/CeO_2$/GNP and CoNiCe/GNP via simple solvothermal method. In order to incorporate CeO_2 as a catalytic activity booster, the atomic ratio is kept at M : Ce = 3:1 (M=Co, Ni). The synthesized catalysts are bifunctional towards ORR and OER and exhibit combination of mass transport and sluggish kinetics. Among them, Co_3O_4/CeO_2/GNP is superior in terms of (1) mass specific activity, (2) onset potential for ORR, (3) half-wave potential, (4) stability surpasses that of Pt/C, and (5) low overpotential for OER, and (6) follows a 4 e^- pathway. A correct combination of the two moieties, viz. Co_3O_4 and CeO_2 could be the most plausible factor behind this catalytic enhancement as is evident from the high ECSA value of Co_3O_4/CeO_2/GNP (198 m^2 g^{-1}) compared to that of Co_3O_4/GNP (24.5 m^2 g^{-1}). This study paves the way to in-depth study of interfaces in Co_3O_4/CeO_2/GNP to uncover the factors affecting above phenomena.

References

[1] Debe, M. K. Electrocatalyst approaches and challenges for automotive fuel cells. *Nature*, 486(7401):43-51, 2012.

[2] Dresp, S., and Strasser, P. Non-noble metal oxides and their application as bifunctional catalyst in reversible fuel cells and rechargeable air batteries. *ChemCatChem*, 10(18):4162-4171, 2018.

[3] Sidhureddy, B., Prins, S., Wen, J., Thiruppathi, A. R., Govindhan, M., and Chen, A. synthesis and electrochemical study of mesoporous nickel-cobalt oxides for efficient oxygen reduction. *ACS Applied Materials & Interfaces*, 11:18295–18304, 2019.

[4] Han, L., Dong, S., and Wang, E. Transition-metal (Co , Ni , and Fe) -based electrocatalysts for the water oxidation reaction. *Advanced Materials*, 28:9266–9291, 2016.

[5] Goswami, C., Hazarika, K. K., Yamada, Y., and Bharali, P. Nonprecious hybrid metal oxide for bifunctional oxygen electrodes: endorsing the role of interfaces in electrocatalytic enhancement. *Energy & Fuels*, 35(16):13370–13381, 2021.

[6] Chutia, B., Patowary, S., Misra, A., Rao, K. N., and Bharali, P. Morphology effect of Co_3O_4 nanooctahedron in boosting oxygen reduction and oxygen evolution reactions. *Energy & Fuels*, 36:13863–13872, 2022.

[7] Montemor, M. F., and Biljana, S. Steps towards highly efficient water splitting and oxygen reduction using nanostructured β-Ni(OH)$_2$. *RSC Advances*, 12:10020–10028, 2022.

[8] Sun, L., Zhou, L., Yang, C., and Yuan, Y. CeO_2 nanoparticle-decorated reduced graphene oxide as an efficient bifunctional electrocatalyst for oxygen reduction and evolution reactions. *International Journal of Hydrogen Energy*, 42(22):15140–15148, 2017.

[9] Khan, S. A., Khan, S. B., and Asiri, A. M. Electro-catalyst based on cerium doped cobalt oxide for oxygen evolution reaction in electrochemical water splitting. *Journal of Materials Science: Materials in Electronics*, 27(5):5294–5302, 2016.

[10] Farjami, A. E. S., and Arvand, S. M. The effect of an anionic surfactant on structure and supercapacitive properties of flower-like nickel oxide. *Journal of Materials Science: Materials in Electronics*, 29(20):17722‒17730, 2018.

[11] Bello, R. H., Coelho, L. A. F., and Becker, D. Role of chemical functionalization of carbon nanoparticles in epoxy matrices. *Journal of Composite Materials*, 52(4):449–464, 2018.

[12] Malard, L. M., Pimenta, M. A., Dresselhaus, G., and Dresselhaus, M. S. Raman spectroscopy in graphene. *Physics Reports*, 473:51‒87, 2009.

[13] Polychronopoulou, K., Alkhoori, A. A., Efstathiou, A. M., Jaoude, M. A., Damaskinos, C. M., Baker, M. A., Almutawa, A., Anjum, D. H., Vasiliades, M. A., Belabbes, A., Vega, L. F., Zedan, A. F., and Hinder, S. J. Design aspects of doped CeO_2 for low-temperature catalytic CO oxidation: transient kinetics and DFT approach. *ACS Applied Materials and Interfaces*, 13(19):22391‒22415, 2021.

[14] Wang, Y., Wei, X., Hu, X., Zhou, W., and Zhao, Y. Effect of formic acid treatment on the structure and catalytic activity of Co_3O_4 for N_2O decomposition. *Catalysis Letters*, 149(4):1026‒1036, 2019.

[15] V G Hadjiev, M. N. I. and I. V. V. The Raman spectra of Co_3O_4. *Journal of Physics C: Solid State Physics*, 21:199‒201, 1988.

[16] Smyrnioti, M., and Ioannides, T. Synthesis of cobalt-based nanomaterials from organic precursors. In. Maaz, K., editor, *Cobalt*, pages 49–69, ISBN:978-953-51-3667-5. IntechOpen, Croatia, 2017.

[17] Dupont, M., Hollenkamp, A. F., and Donne, S. W. Electrochemically active surface area effects on the performance of manganese dioxide for electrochemical capacitor applications. *Electrochimica Acta*, 104:140‒147, 2013.

[18] Chetry, R., Chutia, B., Patowary, S., Borah, B. J., Sudarsanam, P., and Bharali, P. Electronic modulation of Pd/C by simultaneous doping of Cu and Co tendering a highly durable and methanol-tolerant oxygen reduction electrocatalyst. *Energy & Fuels*, 37(13):9557‒9567, 2023.

[19] Githinji, D. N. Digital image analysis for chemical phase identification and particle size determination. *Advances in Physics Theories and Applications*, 45:1‒6, 2015.

[20] Zhang, D., Sun, W., Chen, Z., Zhang, Y., Luo, W., Jiang, Y., and Dou, S. X. Two-dimensional cobalt-/nickel-based oxide nanosheets for high-performance sodium and lithium storage. *Chemistry - A European Journal*, 22(50):18060–18065, 2016.

[21] Zhu, Y., Cao, C., Tao, S., Chu, W., Wu, Z., and Li, Y. Ultrathin nickel hydroxide and oxide nanosheets: synthesis, characterizations and excellent supercapacitor performances. *Scientific Reports*, 4:1–7, 2014.

[22] Luo, Y., Duan, G., and Li, G. Synthesis and characterization of flower-like β-$Ni(OH)_2$ nanoarchitectures. *Journal of Solid State Chemistry*, 180(7):2149–2153, 2007.

[23] Zhou, R., Zheng, Y., Jaroniec, M., and Qiao, S. Z. Determination of the electron transfer number for the oxygen reduction reaction: from theory to experiment. *ACS Catalysis*, 6(7):4720–4728, 2016.

[24] Luo, Y., Wu, Y., Li, B., Mo, T., Li, Y., Feng, S. P., Qu, J., and Chu, P. K. Development and application of fuel cells in the automobile industry. *Journal of Energy Storage*, 42:1–19, 2021.